Design of Planar Parallel Robots With Preloaded Flexures for Guaranteed Backlash Prevention

Wei Wei
e-mail: ww2161@columbia.edu

Nabil Simaan[1]
e-mail: ns2236@columbia.edu

Department of Mechanical Engineering,
Advanced Robotics and Mechanisms
Applications Laboratory (ARMA Lab),
Columbia University,
New York, NY 10027

The precision of parallel robots is limited by backlash in their joints. This paper investigates algorithms for designing inexpensive planar parallel robots with prescribed backlash-free workspace. The method of closing the backlash of the actuators uses preloaded flexible joints to replace the passive joints. These flexible joints may be made using standard joints with preloaded springs or by using preloaded flexure joints. Given a norm-bounded wrench acting on the robot, an algorithm is presented for determining the required preload for the flexible joints in order to guarantee backlash-free operation along a path or within a prescribed workspace. An investigation of the effects of the preloaded flexible joints on the stiffness is carried out using performance measures comparing the same robot with or without preloaded joints. These performance measures use an extended stiffness definition based on three noncollinear vertices on the moving platform. This paper presents simulations of the statics, stiffness, and backlash prevention algorithm, followed by experimental validations. [DOI: 10.1115/1.4000522]

1 Introduction

Parallel robots were initially proposed for spray painting of cars by Pollard [1] in 1942, and the first six-degrees-of-freedom (6DOF) prototype of the Stewart–Gough platform was used as a flight simulator [2]. As the end effector (EE) is simultaneously supported by multiple mechanical legs, parallel robots are well-known for their advantages of providing higher rigidity, higher stiffness, being more compact in structure, and having more payload capacity. One direction of recent developments for parallel robot design is high-precision manufacturing and manipulation, where precision in the order of microns is required from the robot. For this purpose, traditional linear actuators and mechanical joints are not sufficient in providing the necessary accuracy, and joint clearances may cause assembly mode changes [3]. One way to improve precision of linear actuators is to use ball screw slides, which have zero-backlash. However, the use of ball screws increases the costs tremendously. Another alternative to obtain high precision from motors is to use a piezoelectric actuator, as in Refs. [4–6]. But piezo actuators have very limited range of motion and are even more costly than ball screws.

In order to improve the accuracy of mechanical joints, people have developed monolithic flexure joints [7–10]. The use of flexures eliminates all mechanical joints and can therefore provide higher precision [11,12]. For this reason there has been a large body of works on the design of parallel mechanisms using flexure joints [13–19]. However, the limited motion ranges of flexures limit these parallel robots to applications, where small workspace is necessary but high precision is required [18]. Efforts have been made to overcome this limitation by using pseudo-elastic materials [20], distributed elasticity [21,22], and shape optimization for reduced stress concentration [23].

Previous works focused on the use of actuation redundancy [24,25] for stiffness modulation and backlash prevention. Recently, Muller [26] proposed a control method that used actuation redundancy resolution while considering dynamic effects for the purpose of backlash prevention along a specified path. This proposed approach requires solving a quadratic optimization problem, which does not lend itself to fast online computation. Rather than using additional actuators (actuation redundancy) or using offline quadratic optimization methods for backlash prevention, we take a simpler approach by investigating the use of preloaded passive joints in order to prevent the backlash throughout a desired workspace while given a norm-bounded wrench. The advantages of this approach include the simplified design that does not require expensive zero-backlash actuators or actuation redundancy. Also this approach is suitable for miniature parallel robots that use flexures. The determination of preloads results in the robot geometry necessary for backlash prevention.

This paper uses the planar parallel robot (Fig. 1) as a case study to present the backlash prevention algorithm. Upon determining the required preloads to avoid backlash throughout the workspace, stiffness properties of this robot are also presented. Stiffness analysis of robots has been extensively explored [27–33]. As the moving platform is supported by multiple legs, the stiffness of parallel robots is much higher than serial robots. The stiffness matrix is usually derived as a function of the robot Jacobian and stiffness constants of all joints. This paper establishes the complete stiffness model for the proposed parallel robot by taking into account the stiffness of the torsional springs. Moreover, as counterparts of kinematic performance indices, e.g., condition number, kinematic conditioning index (KCI), manipulability [34–37], and so on, stiffness performance indices are proposed to quantitatively evaluate the robot's stiffness properties while taking into account the preload effects of the flexure joints. These proposed indices are utilized to compare the stiffness of the proposed robot to a regular parallel robot without preloads.

The contribution of this paper is in presenting an algorithm for backlash prevention along a specified path and within a desired workspace. This problem is solved for any random norm-bounded wrench acting on the moving platform. The results of this algorithm provide the required preloads of the flexure joints in order to ensure backlash-free operation within the desired workspace. These preload values can be used to design the geometry governing the connection between the flexure joints and the moving platform at the home configuration of the robot.

In addition, the paper presents an investigation on the stiffness effects of adding preloads to the robot and defines novel stiffness performance indices that build on using the vertex velocities of

[1]Corresponding author.

Contributed by the Mechanisms and Robotics Committee of ASME for publication in the JOURNAL OF MECHANISMS AND ROBOTICS. Manuscript received December 16, 2008; final manuscript received July 23, 2009; published online January 11, 2010. Editor: J. Michael McCarthy.

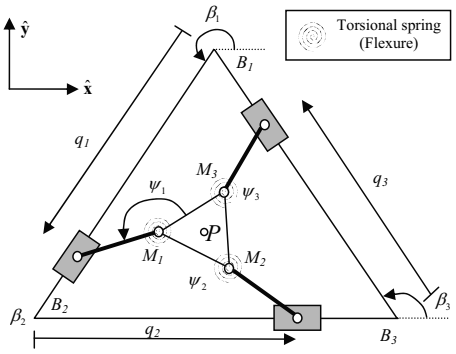

Fig. 1 A 3DOF planar parallel robot with preloaded flexures

three distinct points on the moving platform. The results of our proposed backlash prevention algorithm are simulated and validated experimentally.

In this paper, Sec. 2 presents the problem statement, Sec. 3 presents statics and singularity analysis, Sec. 4 proposes the algorithm to determine the torsional spring preload requirements, Sec. 5 presents the stiffness modeling and introduces stiffness performance indices based on the vertex linear velocity transformation, Secs. 6 and 7 present the simulation and experimental results, respectively, followed by Sec. 8, which concludes and summarizes the proposed work.

2 Problem Statement

As shown in Fig. 1, this PRR planar parallel robot has an equilateral triangular base with linear actuators on the base frame. Three linear sliders move along the frame sides with the positive direction, as defined in Fig. 1. Revolute joints are used to connect the sliders and the legs, as well as the legs and the moving platform. The moving platform is of an equilateral triangular shape, whose geometric center is taken as the EE point of the robot.

Three torsional springs are added to the revolute joints between the moving platform and the legs to provide internal preloads. These springs are assembled coaxially with the revolute joints in order to close the backlash in the linear actuators. This preloading approach provides an inexpensive way of demonstrating the same principle of closing the backlash in the linear actuators by adding preloaded flexure joints.

Three main problems are treated in this paper, as detailed in Secs. 3–5. An overview of the problems is as follows:

P1: Statics is investigated while the robot is assembled with the torsional springs (flexures). Statics ellipsoids are expanded to explore how adding torsional springs affects the robot's statics.

P2: An algorithm is proposed to mathematically determine the preload requirements from the flexure joints, such that the robot is free of backlash along a specific path and within a desired workspace under norm-bounded applied wrench. In Refs. [26,38], for a free actuator, the condition for backlash-free control was given as the magnitude of each control force remaining above a certain level and its sign remaining constant. For the preloaded robot, as shown in Fig. 1, since the slider nut is always preloaded to one side, a different condition is proposed in this paper. Let τ_P denote the actuation force and $\varepsilon > 0$ denote the threshold value, then the backlash-free condition for a linear actuator is $\tau_P > -\varepsilon$, as illustrated in Fig. 2. The physical meaning of this condition is that due to mechanical constraints such as friction and assembly, even if the actuation force changes its direction, the system is still backlash-free as long as this condition is satisfied.

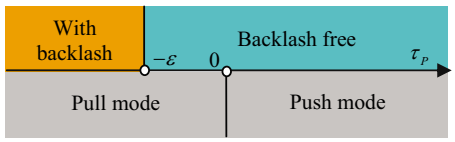

Fig. 2 Explanation of backlash-free condition

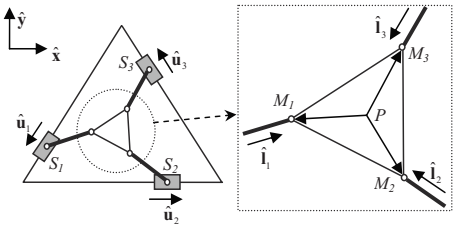

Fig. 3 Kinematic relationship of the planar parallel robot

Mathematically, the backlash-free condition and the norm-bounded constraint are formulated as Eqs. (1) and (2). In Eq. (2), $\mathbf{w}_e$ denotes the wrench applied by the EE to the environment and m denotes its maximal norm

$$\tau_{Pi} + \varepsilon > 0 \tag{1}$$

$$\mathbf{w}_e^T \mathbf{w}_e - m \leq 0 \quad \text{where} \quad \mathbf{w}_e \in \mathbb{R}^{3\times 1} \tag{2}$$

P3: Stiffness modeling is treated mathematically and explicit stiffness matrix is derived. Novel stiffness performance indices are proposed to quantitatively evaluate the robot's stiffness improvement over regular planar parallel robots.

Note that the robot's EE might have a pose change due to the assembly of preloaded springs/flexures. Therefore, the robot should be calibrated after assembly of these preloaded joints. The robot will have definite poses as long as backlash onset is prevented throughout its operation workspace.

3 Statics and Singularity Analysis

For the conventional parallel robot without flexures, as shown in Fig. 1, its Jacobian $\mathbf{J}$ relates the joint speeds $\dot{\mathbf{q}}$ and output twist $\mathbf{t}$ [2], as shown in Eq. (3) [39]. The Jacobian can also be derived through statics analysis (Eq. (4)) [40,41], where $\boldsymbol{\tau}$ represents the actuation forces and $\mathbf{w}_e$ is the applied wrench

$$\mathbf{B}\dot{\mathbf{q}} = \mathbf{A}\mathbf{t}, \quad \dot{\mathbf{q}} = \mathbf{J}\mathbf{t} \quad \text{where} \quad \mathbf{J} = \mathbf{B}^{-1}\mathbf{A} \tag{3}$$

$$\mathbf{B}^{-T}\boldsymbol{\tau} = \mathbf{A}^{-T}\mathbf{w}_e, \quad \boldsymbol{\tau} = \mathbf{J}^{-T}\mathbf{w}_e \quad \text{where} \quad \mathbf{J} = \mathbf{B}^{-1}\mathbf{A} \tag{4}$$

The schematic of the robot is shown in Fig. 3. Conditions of the static equilibrium on the moving platform are expressed in Eq. (5)

$$\underbrace{\begin{bmatrix} (\hat{\mathbf{l}}_1)_2 & (\hat{\mathbf{l}}_2)_2 & (\hat{\mathbf{l}}_3)_2 \\ \hat{\mathbf{z}}^T(\overrightarrow{PM}_1 \times \hat{\mathbf{l}}_1) & \hat{\mathbf{z}}^T(\overrightarrow{PM}_2 \times \hat{\mathbf{l}}_2) & \hat{\mathbf{z}}^T(\overrightarrow{PM}_3 \times \hat{\mathbf{l}}_3) \end{bmatrix}}_{\mathbf{A}^T} \begin{bmatrix} f_1 \\ f_2 \\ f_3 \end{bmatrix} = \begin{bmatrix} \mathbf{f}_e \\ m_e \end{bmatrix} \tag{5}$$

where $\hat{\mathbf{l}}_i$ denotes the unit vectors along the robot legs, $(\hat{\mathbf{l}}_i)_2$ denotes the first two components of $\hat{\mathbf{l}}_i$, $\overrightarrow{PM}_i$ denotes the position vector from the center of the moving platform P to the revolute joints M_i, f_i is the force magnitude along the ith leg, $\mathbf{f}_e$ is the 2D force vector, and m_e is a moment applied by the EE to the environment about $\hat{\mathbf{z}}$. The static equilibrium for each individual leg results in the serial Jacobian matrix as

[2]Throughout this paper, a twist is defined as a three- or six-dimensional column vector with linear velocity preceding the angular velocity.

$$\underbrace{\begin{bmatrix} \hat{\mathbf{u}}_1^T\hat{\mathbf{l}}_1 & 0 & 0 \\ 0 & \hat{\mathbf{u}}_2^T\hat{\mathbf{l}}_2 & 0 \\ 0 & 0 & \hat{\mathbf{u}}_3^T\hat{\mathbf{l}}_3 \end{bmatrix}}_{\mathbf{B}^T}\begin{bmatrix} f_1 \\ f_2 \\ f_3 \end{bmatrix} = \begin{bmatrix} \tau_{P1} \\ \tau_{P2} \\ \tau_{P3} \end{bmatrix} \tag{6}$$

where τ_{Pi} is the force applied to the robot by the linear actuator along unit vector $\hat{\mathbf{u}}_i$. Then the system Jacobian is obtained by using Eq. (4). Note that the Jacobian derived from statics can be used as the kinematic Jacobian only when there is no power loss in the robot.

According to the principle of virtual work, the amount of work done by the external wrench is equal to the work done by the actuators plus the elastic energy stored in the system. Hence Eq. (7) follows

$$\mathbf{w}_e^T\Delta\mathbf{x} = \boldsymbol{\tau}_P^T\Delta\mathbf{q}_P + \boldsymbol{\tau}_S^T\Delta\boldsymbol{\psi} \tag{7}$$

where $\mathbf{x}$ is the position and orientation vector of the EE, $\Delta\mathbf{x}$ represents the variation in $\mathbf{x}$, $\Delta\mathbf{q}_P$ represents the changes in joint positions, and $\Delta\boldsymbol{\psi}$ measures the changes in the flexures (spring-loaded joints). From the geometry of the robot, for the ith leg, Eq. (8) follows

$$\mathbf{s}_i = \mathbf{p} + \overrightarrow{PM}_i + \overrightarrow{M_iS_i} \tag{8}$$

Taking the variations of Eq. (8) and expressing $\Delta\boldsymbol{\psi}$ in terms of $\Delta\mathbf{q}_P$ yields

$$\Delta\boldsymbol{\psi} = \underbrace{\mathbf{J}_{\psi q1}^{-1}(\mathbf{J}_{\psi q2} - \mathbf{J}_{\psi q3}\mathbf{J}^{-1})}_{\mathbf{J}_{\psi q}}\Delta\mathbf{q}_P \tag{9}$$

where

$$\mathbf{J}_{\psi q1} = \begin{bmatrix} -l\sin(\psi_1+\theta) & 0 & 0 \\ 0 & -l\sin\left(\psi_2+\frac{2\pi}{3}+\theta\right) & 0 \\ 0 & 0 & -l\sin\left(\psi_3+\frac{4\pi}{3}+\theta\right) \end{bmatrix} \tag{10}$$

$$\mathbf{J}_{\psi q2} = \begin{bmatrix} \cos(\beta_1) & 0 & 0 \\ 0 & \cos(\beta_2) & 0 \\ 0 & 0 & \cos(\beta_3) \end{bmatrix} \tag{11}$$

$$\mathbf{J}_{\psi q3} = \begin{bmatrix} 1 & 0 & -\left[r\sin\left(\theta+\frac{5\pi}{6}\right)+l\sin(\psi_1+\theta)\right] \\ 1 & 0 & -\left[r\sin\left(\theta+\frac{9\pi}{6}\right)+l\sin\left(\psi_2+\frac{2\pi}{3}+\theta\right)\right] \\ 1 & 0 & -\left[r\sin\left(\theta+\frac{\pi}{6}\right)+l\sin\left(\psi_3+\frac{4\pi}{3}+\theta\right)\right] \end{bmatrix} \tag{12}$$

In Eqs. (10) and (12), θ denotes the orientation of the moving platform in the world coordinate system, l denotes the length of legs, and r denotes the radius of the moving platform.

Substituting Eq. (9) in Eq. (7) and applying the Jacobian results in

$$\mathbf{w}_e^T\Delta\mathbf{x} = \boldsymbol{\tau}_P^T\mathbf{J}\Delta\mathbf{x} + \boldsymbol{\tau}_S^T\mathbf{J}_{\psi q}\mathbf{J}\Delta\mathbf{x} \tag{13}$$

Canceling $\Delta\mathbf{x}$ from both sides of Eq. (13) and taking transpose of the results yields

$$\mathbf{w}_e = \mathbf{J}^T\boldsymbol{\tau}_P + \mathbf{J}^T\mathbf{J}_{\psi q}^T\boldsymbol{\tau}_S = \mathbf{J}^T(\boldsymbol{\tau}_P + \mathbf{J}_{\psi q}^T\boldsymbol{\tau}_S) \tag{14}$$

Recall that Eq. (15) gives the statics relation of a parallel robot while having no internal preloaded flexures

$$\mathbf{w}_e = \mathbf{J}^T\boldsymbol{\tau}_P \tag{15}$$

Equation (14) differs from Eq. (15) by the term $\mathbf{J}^T\mathbf{J}_{\psi q}^T\boldsymbol{\tau}_S$. At a given configuration, the kinematics of the robot is easy to solve; hence, Jacobian $\mathbf{J}_{\psi q}$ is known. From the geometry of the spring joints, the torsions $\boldsymbol{\tau}_S$ are easy to solve via linear relationship for known spring constants. Therefore, the statics of preloaded parallel robots follows the same solution procedure as for a traditional parallel robot. However, for the case of preloaded parallel robots, the duality of robot Jacobian $\mathbf{J}$ between kinematics and statics, as in Eqs. (3) and (4), does not hold any more because part of the work done by the actuators is stored as the elastic energy in the springs.

Singularity is an attribute associated with a robot once its structure is determined. Although the addition of torsional springs does not change the robot's kinematic structure, it does change the statics, as observed in Eq. (14). Therefore, it is expected that the torsional springs can be utilized to avoid singularity or increase the nonsingular workspace of the robot from a statics viewpoint.

For a traditional parallel robot without the torsional springs, the actuation force ellipsoid is expressed as

$$\mathbf{w}_e^T\mathbf{w}_e = \boldsymbol{\tau}_P^T\mathbf{J}\mathbf{J}^T\boldsymbol{\tau}_P = 1 \tag{16}$$

For a parallel robot with the torsional spring, based on Eq. (14), the actuation force ellipsoid is expressed as

$$\mathbf{w}_e^T\mathbf{w}_e = (\boldsymbol{\tau}_P^T + \boldsymbol{\tau}_S^T\mathbf{J}_{\psi q})\mathbf{J}\mathbf{J}^T(\boldsymbol{\tau}_P + \mathbf{J}_{\psi q}^T\boldsymbol{\tau}_S) = 1 \tag{17}$$

Expanding Eq. (17) yields

$$\mathbf{w}_e^T\mathbf{w}_e = \boldsymbol{\tau}_P^T\mathbf{J}\mathbf{J}^T\boldsymbol{\tau}_P + \boldsymbol{\tau}_S^T\mathbf{J}_{\psi q}\mathbf{J}\mathbf{J}^T\mathbf{J}_{\psi q}^T\boldsymbol{\tau}_S + 2\boldsymbol{\tau}_P^T\mathbf{J}\mathbf{J}^T\mathbf{J}_{\psi q}^T\boldsymbol{\tau}_S \tag{18}$$

where the intermediate terms of the expansion are combined since the transpose of a scalar is equal to itself. Defining $\mathbf{a}=\mathbf{J}^T\boldsymbol{\tau}_P$ and $\mathbf{b}=\mathbf{J}^T\mathbf{J}_{\psi q}^T\boldsymbol{\tau}_S$, Eq. (18) becomes $\mathbf{w}_e^T\mathbf{w}_e=\mathbf{a}^T\mathbf{a}+\mathbf{b}^T\mathbf{b}+2\mathbf{a}^T\mathbf{b}$, where the term $2\mathbf{a}^T\mathbf{b}$ corresponds to $2\boldsymbol{\tau}_P^T\mathbf{J}\mathbf{J}^T\mathbf{J}_{\psi q}^T\boldsymbol{\tau}_S$. Since $\mathbf{w}_e^T\mathbf{w}_e\geq 0$, the term $2\mathbf{a}^T\mathbf{b}$ cannot be dominant compared with the first two positive semidefinite terms $\mathbf{a}^T\mathbf{a}+\mathbf{b}^T\mathbf{b}$. In addition, Eq. (18) has one design vector $\boldsymbol{\tau}_S$ that controls the terms $\mathbf{b}^T\mathbf{b}$ and $2\mathbf{a}^T\mathbf{b}$ in Eq. (18). Therefore, we choose to investigate and plot the individual force ellipsoids stemming from the terms $\mathbf{a}^T\mathbf{a}$ and $\mathbf{b}^T\mathbf{b}$ in the numerical simulation of Sec. 6.1.

4 Preloads Determination for Backlash Avoidance

This section focuses on proposing the algorithm to determine the preload requirements of the flexures for a specific path and within a desired workspace while the robot is under a norm-bounded applied wrench.

4.1 Path-Dependent Preload Determination. In this subsection, a path is prespecified for the EE to trace. The preload requirements are determined such that the robot is backlash-free

while tracing this path. The proposed algorithm is applicable to any specified path, and is easy to implement for a given task. The algorithm is still based on the 3DOF parallel robot with flexures, as shown in Fig. 1.

Assume all forces are defined as applied on the robot. The principle of virtual work (Eq. (7)) becomes Eq. (19), where $\mathbf{w}_e'$ denotes the wrench applied by the environment to the robot

$$\mathbf{w}_e'^T \Delta\mathbf{x} + \boldsymbol{\tau}_P^T \Delta\mathbf{q}_P + \boldsymbol{\tau}_S^T \Delta\boldsymbol{\psi} = 0 \tag{19}$$

Substituting in the Jacobian relationships and canceling $\Delta\mathbf{x}$ from both sides yields

$$\mathbf{w}_e' + \mathbf{J}^T \boldsymbol{\tau}_P + \mathbf{J}^T \mathbf{J}_{\psi q}^T \boldsymbol{\tau}_S = 0 \tag{20}$$

With the assumption that the flexure joints are linear torsional springs, the relationship of Eq. (21) follows

$$\boldsymbol{\tau}_S = \underbrace{\begin{bmatrix} K_S & 0 & 0 \\ 0 & K_S & 0 \\ 0 & 0 & K_S \end{bmatrix}}_{\mathbf{K}_S} \begin{bmatrix} \Delta\zeta_1 \\ \Delta\zeta_2 \\ \Delta\zeta_3 \end{bmatrix} \tag{21}$$

In Eq. (21), $\Delta\zeta_i$ is defined as the joint angle measured from its neutral configuration. $K_S \Delta\zeta_i$ physically denotes the torsion generated by the flexure at the current configuration. The value of $\Delta\zeta_i$ is to be solved in order to determine the preload condition. Substituting Eq. (21) in Eq. (20) and solving for $\Delta\boldsymbol{\zeta}$ gives

$$\begin{aligned} \Delta\boldsymbol{\zeta} &= -(\mathbf{J}^T \mathbf{J}_{\psi q}^T \mathbf{K}_S)^{-1} (\mathbf{w}_e' + \mathbf{J}^T \boldsymbol{\tau}_P) \\ &= \underbrace{[-\mathbf{K}_S^{-1} \mathbf{J}_{\psi q}^{-T} - (\mathbf{J}^T \mathbf{J}_{\psi q}^T \mathbf{K}_S)^{-1}]}_{\mathbf{Q}} \underbrace{\begin{bmatrix} \boldsymbol{\tau}_P \\ \mathbf{w}_e' \end{bmatrix}}_{\boldsymbol{\eta}} \end{aligned} \tag{22}$$

The minimum preload requirements are to be solved to close the backlash. Therefore, a scalar cost function $F=$ is defined as Eq. (23), which physically represents the elastic energy stored in the robot

$$F = \frac{1}{2} \Delta\boldsymbol{\zeta}^T \mathbf{K}_S \Delta\boldsymbol{\zeta} = \frac{1}{2} \boldsymbol{\eta}^T \underbrace{\mathbf{Q}^T \mathbf{K}_S \mathbf{Q}}_{\mathbf{Q}_F} \boldsymbol{\eta} = \frac{1}{2} \boldsymbol{\eta}^T \mathbf{Q}_F \boldsymbol{\eta} \tag{23}$$

Function F is subject to four constraints as introduced in Eqs. (1) and (2). Using matrix notations to introduce vector $\boldsymbol{\eta}$ into the constraints, Eqs. (1) and (2) are rewritten as

$$\frac{1}{2} (\mathbf{A}_i \boldsymbol{\eta} + \mathbf{A}_i \boldsymbol{\varepsilon})^T (\mathbf{A}_i \boldsymbol{\eta} + \mathbf{A}_i \boldsymbol{\varepsilon}) > 0 \tag{24}$$

$$\frac{1}{2} [(\mathbf{B}\boldsymbol{\eta})^T (\mathbf{B}\boldsymbol{\eta}) - m] \leq 0 \tag{25}$$

where $\mathbf{A}_i = \text{diag}(\delta_{ij})_{6\times 6}$ $(i=1,\ldots,3)$ for each $i,j=1\ldots6$, and $\mathbf{A}_i^T \mathbf{A}_i = \mathbf{A}_i$. $\mathbf{B} = \begin{bmatrix} \mathbf{0}_{3\times3} & \mathbf{0}_{3\times3} \\ \mathbf{0}_{3\times3} & \mathbf{I}_3 \end{bmatrix}$ and $\mathbf{B}^T\mathbf{B} = \mathbf{B}$. $\boldsymbol{\varepsilon} = [\varepsilon \ \varepsilon \ \varepsilon \ 0 \ 0 \ 0]^T$. Then the minimization problem is formulated as a Lagrange problem with inequality constraints, also known as Karush–Kuhn–Tucker (KKT) conditions [42]. All inequality conditions are incorporated into the Lagrangian as equalities by adding the slack variable s_i, and thus the Lagrangian is obtained by using four multipliers as in Eq. (26).

$$\begin{aligned} L = \frac{1}{2} \Bigg\{ & \boldsymbol{\eta}^T \mathbf{Q}_F \boldsymbol{\eta} + \sum_{i=1}^{3} \lambda_i [(\mathbf{A}_i \boldsymbol{\eta} + \mathbf{A}_i \boldsymbol{\varepsilon})^T (\mathbf{A}_i \boldsymbol{\eta} + \mathbf{A}_i \boldsymbol{\varepsilon}) - s_i^2] \\ & + \lambda_4 [(\mathbf{B}\boldsymbol{\eta})^T (\mathbf{B}\boldsymbol{\eta}) - m + s_4^2] \Bigg\} \end{aligned} \tag{26}$$

Expanding the Lagrangian yields

$$\begin{aligned} L = \frac{1}{2} \Bigg[& \boldsymbol{\eta}^T \mathbf{Q}_F \boldsymbol{\eta} + \lambda_4 (\boldsymbol{\eta}^T \mathbf{B} \boldsymbol{\eta} - m + s_4^2) + \sum_{i=1}^{3} (\lambda_i \boldsymbol{\eta}^T \mathbf{A}_i \boldsymbol{\eta} + \lambda_i \boldsymbol{\varepsilon}^T \mathbf{A}_i \boldsymbol{\eta} \\ & + \lambda_i \boldsymbol{\eta}^T \mathbf{A}_i \boldsymbol{\varepsilon} + \lambda_i \boldsymbol{\varepsilon}^T \mathbf{A}_i \boldsymbol{\varepsilon} - \lambda_i s_i^2) \Bigg] \end{aligned} \tag{27}$$

Finding the partial derivatives of L with respect to $\boldsymbol{\eta}$, λ_i and s_i results in

$$\frac{\partial L}{\partial \boldsymbol{\eta}} = \mathbf{Q}_F \boldsymbol{\eta} + \sum_{i=1}^{3} (\lambda_i \mathbf{A}_i \boldsymbol{\eta} + \lambda_i \mathbf{A}_i \boldsymbol{\varepsilon}) + \lambda_4 \mathbf{B} \boldsymbol{\eta} = 0 \tag{28}$$

$$\frac{\partial L}{\partial \lambda_i} = g_i(\boldsymbol{\eta}) - s_i^2 = 0 \tag{29}$$

$$\frac{\partial L}{\partial s_i} = \lambda_i s_i = 0 \tag{30}$$

where $\mathbf{g}(\boldsymbol{\eta})$ denotes the vector of constraint equations, as in Eqs. (24) and (25). This system has 14 equations and 14 unknowns. The minimization problem is solved by assuming all s_i's are equal to zero. Note that under this assumption, the resulting minimal value of the cost function F is not necessarily the global minimum, but rather a local minimum. However, as long as there is a solution, it can be used to solve for $\Delta\boldsymbol{\zeta}$ from Eq. (22). The resulting preload requirements, although may not be the smallest possible values, are guaranteed to satisfy backlash-free conditions by virtue of the KKT theorem.

By using the Lagrangian approach, the entire specified path is scanned such that the minimum torsional preloads for all configurations are determined. Hence, three vectors of $\Delta\boldsymbol{\zeta}_i$ are obtained, each corresponding to all minimal preload requirements of one joint along the path. During the path scan, the geometric range of joint variation is also obtained. Then the following algorithm is applied to solve for initial preloads:

- Vectors $\Delta\boldsymbol{\zeta}_i$ are solved from Eq. (22) and $\max(\Delta\boldsymbol{\zeta}_i)$ is obtained for each leg.
- $K_S \max(\Delta\boldsymbol{\zeta}_i)$ is specified to be the preload of flexure joint i when the joint has minimum actual torsion. In other words, within the range of the flexure joint motion, the orientation that has the smallest actual flexural torsion is specified to have the maximum preload value solved from the Lagrangian problem for the specified path.
- All flexure joints are preloaded from the starting configuration. The determination of how much to preload is calculated via Eq. (31). Note that ψ_i^1 means the starting joint angle along the path and $\psi_i^{\max}$ denotes the maximum angle of rotation.
- Finally, the governing geometry between the flexure joints and the moving platform is determined for the robot

$$K_S \Delta\zeta_{i\_\text{preload}} = K_S \max(\Delta\boldsymbol{\zeta}_i) + K_S(\psi_i^{\max} - \psi_i^1) \tag{31}$$

While the leg moves in the range of motion for the given task, the actual torque of the flexure will be guaranteed to be greater than or equal to the value solved from the Lagrangian problem for each configuration. Therefore, the backlash-free conditions will always be satisfied. Numerical simulations and experiments will be presented to verify the algorithm in Secs. 6 and 7.

4.2 General Preload Determination Within the Workspace. In Sec. 4.1, the problem of preload determination was treated along a specified path. A further problem to be solved is to find global preloads suitable for the robot to avoid backlash throughout the desired workspace.

Assume the orientation of the EE is fixed, meaning that the EE only translates in the workspace without rotation. From the center

point of the triangle frame, the workspace is divided into a series of concentric circular bands, with very thin width. Each band can be considered as a specified path for the robot to trace, as in Sec. 4.1. Notice that the forces to close backlash of the linear actuators are provided by the flexure joints. The closer a leg is to the base frame, the more preload is required from the flexure to close the backlash. Hence, while tracing different sliced circle bands of the workspace, the largest one will provide larger preload requirements compared with inner circles. It means that with the preloads determined from the largest circle, the robot will have no backlash within the area. Therefore, a circle, or more generally, a geometric path can be found, which encompasses the specific workspace of interest. After determining the preload requirements along this path, the system is ensured to close the backlash throughout the desired workspace.

5 Stiffness Analysis

5.1 Stiffness Modeling. Stiffness modeling for robots with flexible components have been investigated in [31–33]. To model the stiffness of the robot, the basic relationship is

$$\mathbf{K} = \frac{\partial \mathbf{w}_e}{\partial \mathbf{x}} \tag{32}$$

Substituting Eq. (14) into Eq. (32) yields

$$\mathbf{K}_{\text{flex}} = \frac{\partial[\mathbf{J}^T(\boldsymbol{\tau}_P + \mathbf{J}_{\psi q}^T \boldsymbol{\tau}_S)]}{\partial \mathbf{x}} \tag{33}$$

The second-order kinematic derivatives of Eq. (33) can be neglected for robots with nonbackdrivable active joints [43]. Therefore, Eq. (33) simplifies to

$$\mathbf{K}_{\text{flex}} = \mathbf{J}^T\left(\frac{\partial \boldsymbol{\tau}_P}{\partial \mathbf{x}} + \mathbf{J}_{\psi q}^T \frac{\partial \boldsymbol{\tau}_S}{\partial \mathbf{x}}\right) \tag{34}$$

The partial derivatives in Eq. (34) are expressed as

$$\frac{\partial \boldsymbol{\tau}_P}{\partial \mathbf{x}} = \frac{\partial \boldsymbol{\tau}_P}{\partial \mathbf{q}} \frac{\partial \mathbf{q}}{\partial \mathbf{x}} = \mathbf{K}_P \mathbf{J} \tag{35}$$

$$\frac{\partial \boldsymbol{\tau}_S}{\partial \mathbf{x}} = \frac{\partial \boldsymbol{\tau}_S}{\partial \boldsymbol{\psi}} \frac{\partial \boldsymbol{\psi}}{\partial \mathbf{q}} \frac{\partial \mathbf{q}}{\partial \mathbf{x}} = \mathbf{K}_S \mathbf{J}_{\psi q} \mathbf{J} \tag{36}$$

Substituting Eqs. (35) and (36) into Eq. (34) yields the expression of the stiffness matrix

$$\mathbf{K}_{\text{flex}} = \mathbf{J}^T \mathbf{K}_P \mathbf{J} + \mathbf{J}^T \mathbf{J}_{\psi q}^T \mathbf{K}_S \mathbf{J}_{\psi q} \mathbf{J} \tag{37}$$

5.2 Stiffness Performance Indices. To quantify the effects of the flexure joints on the robot stiffness characteristics, we use several performance measures based on the stiffness, as defined in Eq. (37).

Well-accepted kinematic performance indices include manipulability ellipsoids, manipulability polytopes, isotropy measures, kinematic conditioning, and dexterity [34–37,44–50]. In evaluating KCI or manipulability, due to inhomogeneity of dimensions associated with linear and angular speeds, the characteristic length [34] was introduced to obtain a dimensionless Jacobian. A kinematic performance index provides designers a scalar measure of the robot's performance, and therefore, guides the dimensional synthesis. In this subsection, stiffness performance indices are proposed as counterparts for kinematic performance measures. These indices are used to evaluate the stiffness effects of adding the flexures to the robot.

Before presenting the specific stiffness performance indices, the problem of inhomogeneous physical units associated with kinematics and stiffness is revisited. Equations (38) and (39) recall the Jacobian and stiffness relationships for the proposed 3DOF parallel robot, with all units explicitly written.

$$\Delta \mathbf{q} = \mathbf{J} \Delta \mathbf{x} \quad \text{where} \quad \begin{bmatrix} \text{m} \\ \text{m} \\ \text{m} \end{bmatrix} = \begin{bmatrix} 1 & 1 & \text{m} \\ 1 & 1 & \text{m} \\ 1 & 1 & \text{m} \end{bmatrix} \begin{bmatrix} \text{m} \\ \text{m} \\ 1 \end{bmatrix} \tag{38}$$

$$\Delta \mathbf{w}_e = \mathbf{K} \Delta \mathbf{x} \quad \text{where} \quad \begin{bmatrix} \text{N} \\ \text{N} \\ \text{N m} \end{bmatrix} = \begin{bmatrix} \text{N/m} & \text{N/m} & \text{N} \\ \text{N/m} & \text{N/m} & \text{N} \\ \text{N} & \text{N} & \text{N m} \end{bmatrix} \begin{bmatrix} \text{m} \\ \text{m} \\ 1 \end{bmatrix} \tag{39}$$

It is clear that the components of the Jacobian bear two different units, while the components of the stiffness matrix bear three different units. The reason for this unit inhomogeneity is the difference in units of linear and angular velocities, and the difference in units between forces and moments.

To accommodate this inhomogeneity, the technique of vertex velocity transformation is used [34]. The basic idea is to use the linear velocities of three noncollinear points on the moving platform to represent the EE twist, and therefore eliminate the inhomogeneity of units in the twist. The detailed derivation is omitted in this paper, and some intermediate steps, which were not explicitly shown in Ref. [34], are given here.

Let $\Delta \mathbf{m}_i$ denote the linear velocity variation in the connection point between the moving platform and the ith leg. The final transformation is derived as

$$(\Delta \mathbf{x})_6 = \begin{bmatrix} \frac{1}{3}\begin{bmatrix} \mathbf{I}_{3\times 3} & \mathbf{I}_{3\times 3} & \mathbf{I}_{3\times 3} \end{bmatrix} \\ \mathbf{D}^{-1}\mathbf{C}_{3\times 9} \end{bmatrix} \begin{bmatrix} \Delta \mathbf{m}_1 \\ \Delta \mathbf{m}_2 \\ \Delta \mathbf{m}_3 \end{bmatrix} \tag{40}$$

where $(\Delta \mathbf{x})_6$ denotes the 6D twist vector. For an equilateral moving platform, the matrix $\mathbf{C}$ is given as

$$\mathbf{C}_{3\times 9} = \frac{1}{6}\begin{bmatrix} 0 & 1 & -1 & 0 & 1 & 2 & 0 & -2 & -1 \\ -1 & 0 & -2 & -1 & 0 & 1 & 2 & 0 & 1 \\ 1 & 2 & 0 & -2 & -1 & 0 & 1 & -1 & 0 \end{bmatrix}$$

$$\mathbf{D} \equiv \frac{1}{2}[\text{trace}(\mathbf{P})\mathbf{I}_{3\times 3} - \mathbf{P}] \quad \text{and} \quad \mathbf{P} \equiv \begin{bmatrix} \mathbf{m}_1 - \mathbf{p} & \mathbf{m}_2 - \mathbf{p} & \mathbf{m}_3 - \mathbf{p} \end{bmatrix}$$

For the planar robot case, the 6D twist is transformed to 3D as

$$\Delta \mathbf{x} = \begin{bmatrix} 1 & 0 & 0 & 0 & 0 & 0 \\ 0 & 1 & 0 & 0 & 0 & 0 \\ 0 & 0 & 0 & 0 & 0 & 1 \end{bmatrix} (\Delta \mathbf{x})_6 \tag{41}$$

After substituting Eqs. (40) and (41) in Eq. (37), an expression for the homogeneous stiffness matrix $\tilde{\mathbf{K}}$ is obtained such that

$$\Delta \mathbf{w}_e = \tilde{\mathbf{K}} \Delta \mathbf{m} \tag{42}$$

The stiffness performance indices defined in Table 1 quantify the percentage improvement in the robot stiffness performance as a result of adding the flexure joints.

The indices in Table 1 follow the definitions of kinematic performance metrics, but use the stiffness matrix instead of using the kinematics Jacobian. Index 1 quantifies the improvement in the Frobenius norm of the stiffness matrix. Index 2 extends the definition of the kinematic manipulability. This index is directly related to index 3, which measures the increase in the volume of the stiffness ellipsoid. Both indices 2 and 3 take into account the minimal singular value of the stiffness matrix. Index 4 measures the isotropy of the stiffness ellipsoid. We note that by using the twist transformation $\Delta \mathbf{x} \rightarrow \Delta \mathbf{m}$, the need for using a characteristic length is mitigated while evaluating the translational stiffness performance and the rotational stiffness performance.

Table 1 Stiffness performance indices

Index 1	$\mathrm{SPI}_1 = \dfrac{\|\tilde{\mathbf{K}}_{\mathrm{with}}\tilde{\mathbf{K}}_{\mathrm{with}}^T\|}{\|\tilde{\mathbf{K}}_{\mathrm{without}}\tilde{\mathbf{K}}_{\mathrm{without}}^T\|} - 1$
Index 2	$\mathrm{SPI}_2 = \dfrac{\sqrt{\det(\tilde{\mathbf{K}}_{\mathrm{with}}\tilde{\mathbf{K}}_{\mathrm{with}}^T)}}{\sqrt{\det(\tilde{\mathbf{K}}_{\mathrm{without}}\tilde{\mathbf{K}}_{\mathrm{without}}^T)}} - 1$
Index 3	$\mathrm{SPI}_3 = \dfrac{V_E(\tilde{\mathbf{K}}_{\mathrm{with}})}{V_E(\tilde{\mathbf{K}}_{\mathrm{without}})} - 1$
Index 4	$\mathrm{SPI}_4 = \dfrac{\sigma_{\min}(\tilde{\mathbf{K}}_{\mathrm{with}})}{\sigma_{\max}(\tilde{\mathbf{K}}_{\mathrm{with}})} \cdot \dfrac{\sigma_{\max}(\tilde{\mathbf{K}}_{\mathrm{without}})}{\sigma_{\min}(\tilde{\mathbf{K}}_{\mathrm{without}})} - 1$

6 Simulations

6.1 Statics and Singularity. Equations (14) and (15) show the difference in the robot statics as a result of adding flexure joints. In this subsection, we investigate the statics of the robot as it traverses a path approaching a singularity, as shown in Fig. 4. In the simulation, we assume the triangular base radius is 200 mm and the moving platform radius is 30 mm. The length of the robot leg is 90 mm. A path starting from $[20\ \mathrm{mm},\ 0,\ 0]^T$ and ending at $[-5\ \mathrm{mm},\ 0,\ 0]^T$ is designed for the robot to trace such that as the robot moves along the path, it is getting closer to the singular configuration.

The following plot (Fig. 5(*a*)) shows all statics ellipses along the path. Note that the inner ones represent the ellipses associated with $\boldsymbol{\tau}_P^T\mathbf{J}\mathbf{J}^T\boldsymbol{\tau}_P$ and the outer ones represent the additional ellipses generated by $\boldsymbol{\tau}_S^T\mathbf{J}_{\psi q}\mathbf{J}\mathbf{J}^T\mathbf{J}_{\psi q}^T\boldsymbol{\tau}_S$ in Eq. (18).

It is seen that as the robot gets closer to the singular configuration both ellipses tend to be singular. However, the directions of the major and minor axes of both ellipses do not coincide (Fig. 5(*c*)). This disagreement can be utilized such that the robot, while in the neighborhood of a singularity, can withstand applied wrench from any arbitrary direction. In this sense, the static conditioning of the robot in the neighborhood of a singularity can be improved, as shown in Fig. 6.

Figure 6(*a*) shows that the manipulability ratio between $\mathbf{J}^T\mathbf{J}_{\psi q}^T$ and $\mathbf{J}^T$ is in the order of 10^3. Moreover, as the robot gets closer to the singular configuration, the ratio increases faster than at the beginning. This is because the ellipse of matrix $\mathbf{J}^T$ degenerates to a line faster than the ellipse of matrix $\mathbf{J}^T\mathbf{J}_{\psi q}^T$. In Fig. 6(*b*), it is seen

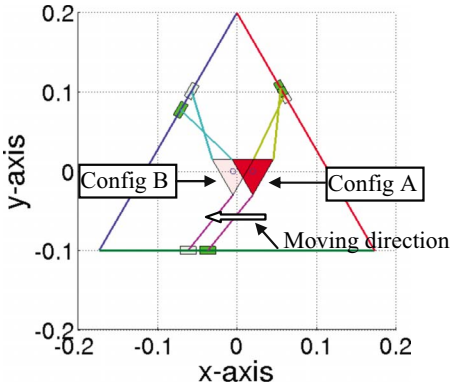

Fig. 4 Designed path from configuration A to configuration B where configuration B approaches singularity

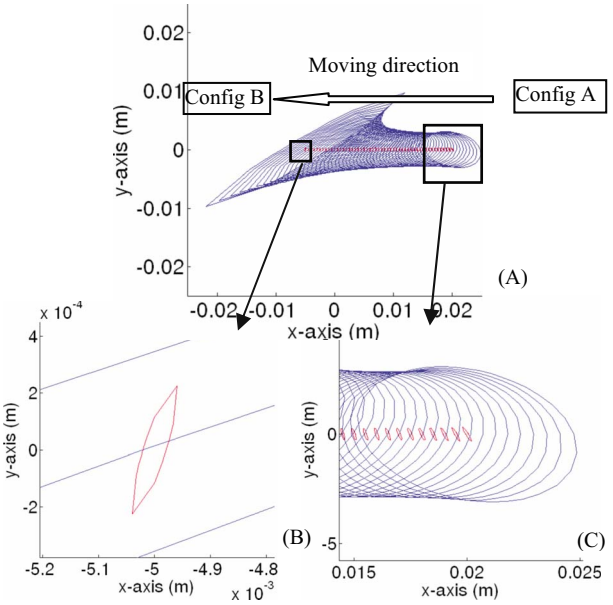

Fig. 5 Statics ellipses along the path of Fig. 4

that the ellipse of matrix $\mathbf{J}^T\mathbf{J}_{\psi q}^T$ is always more isotropic than that of matrix $\mathbf{J}^T$. Even in the neighborhood of the singularity, the matrix $\mathbf{J}^T\mathbf{J}_{\psi q}^T$ becomes singular slower than $\mathbf{J}^T$.

6.2 Preload Determination

6.2.1 Path-Based Preload Determination. Based on the discussion in Sec. 4, the preload determination for a specific path and for a desired workspace is simulated in this subsection. The simulation assumptions are as follows:

1. The base radius is 100 mm. The moving platform radius is 30 mm. The leg length is 50 mm.
2. A circular path of 10 mm radius is traced. This circle is centered at the geometric center of the base triangle. The starting point of the path has coordinates of $[10\ \mathrm{mm},\ 0,\ 0]^T$, and the path goes in the counterclockwise direction.
3. The applied wrench is assumed to be $[1\ \mathrm{N},\ 1\ \mathrm{N},\ 1\ \mathrm{N\,m}]^T$, meaning the threshold boundary value m is 3, as in Eq. (2).
4. The backlash-free condition is that $\tau > -1$, where $\varepsilon = 1$.
5. The torsional spring constant is assumed to be 1 N m/rad.

By applying the proposed algorithm, the preloads are solved as (see Table 2):

With these preloads, all points along this path are verified to

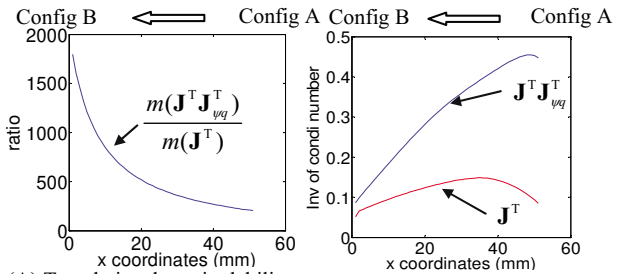

(A) Translational manipulability ratio between $\mathbf{J}^T\mathbf{J}_{\psi q}^T$ and $\mathbf{J}^T$.

(B) The inverse of condition number for $\mathbf{J}^T\mathbf{J}_{\psi q}^T$ and $\mathbf{J}^T$.

Fig. 6 Manipulability ratio and inverse of condition number along the path from configuration A to configuration B of Fig. 4

Table 2 Preload values for the torsional springs

	Spring 1	Spring 2	Spring 3
Preload values (N m)	0.6048	0.8102	0.9913

satisfy the zero-backlash condition. The minimum actuation forces are 15.65 N, 13.88 N, and 14.83 N, respectively. Note that the solid line denotes actuator 1, the dotted line denotes actuator 2, and the dashed line denotes actuator 3 (Fig. 7).

Since in the Lagrange equation the minimization problem was subject to an inequality condition as in Eq. (2), it is expected that for any wrench with norm smaller or equal to the specified value, the algorithm still holds. This is verified that under a newly applied wrench of $[0\ \text{N},\ 0\ \text{N},\ 1.73\ \text{N m}]^T$, the actuation forces still satisfy the backlash-free condition, as shown in Fig. 8(*a*). Note that with the wrench norm being 1.73 this new wrench maximally balances the preload effects on the actuators and hence requires the smallest actuation forces.

The proposed algorithm is conservative and results in a robot that can close the backlash even if $\|\mathbf{w}_e\|$ is greater than the specified norm. Figure 8(*b*) shows the robot's margin of avoiding backlash, where the boundary norm for the applied wrench is calculated as 2.29. Figure 8(*c*) shows that once the applied wrench is beyond the boundary norm, backlash will be triggered in the robot.

6.2.2 Workspace-Based Preload Determination. As proposed in Sec. 4.2, for a desired workspace, an encompassing path needs to be traced to determine preload requirements, which are expected to satisfy all points within this workspace. Assume that the workspace inside the circle of 10 mm radius is of interest. Different circles within this workspace radius from 2 mm to 10 mm are traced, with an increment of 2 mm. The required preloads from the springs are listed below in Table 3. All other assumptions remain the same.

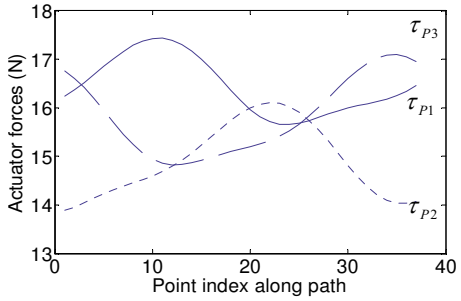

Fig. 7 Actuation force plots as the robot traces a circular path

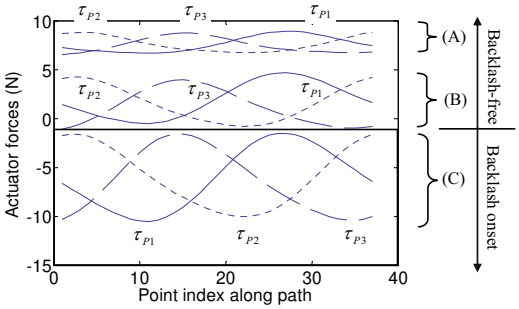

Fig. 8 Actuation force plots with different wrenches of (*a*) $[0\ \text{N},\ 0\ \text{N},\ 1.73\ \text{N m}]^T$, (*b*) $[0\ \text{N},\ 0\ \text{N},\ 2.29\ \text{N m}]^T$, and (*c*) $[0\ \text{N},\ 0\ \text{N},\ 3\ \text{N m}]^T$. The shaded region has the actuator backlash onset.

Table 3 Required spring preloads for different tracing paths

	Spring 1	Spring 2	Spring 3
2 mm circular path (N m)	0.5609	0.5992	0.6366
4 mm circular path (N m)	0.5734	0.6512	0.7254
6 mm circular path (N m)	0.5851	0.7036	0.8140
8 mm circular path (N m)	0.5956	0.7566	0.9026
10 mm circular path (N m)	0.6048	0.8102	0.9913

Table 3 shows increased preload requirements as the workspace radius increases. With the preloads determined by the circular path of 10 mm radius, the whole workspace is checked for the backlash-free condition. It is easily verified that the robot has no backlash from the actuators at all points within the workspace. On the other hand, the preloads determined by the 2 mm circle are used to trace the 10 mm circle with applied wrench $[0\ \text{N},\ 0\ \text{N},\ 1.73\ \text{N m}]^T$. Figure 9 shows the required actuation forces, where the minimal values are −2.45 N, −5.26 N, and 1.12 N for actuators 1, 2, and 3, respectively. It is obvious that actuators 1 and 2 will suffer from backlash onset.

6.3 Stiffness. For this simulation, it is assumed that the robot is tracing the same circular path of 10 mm radius about the central point of its workspace. The stiffness matrix $\mathbf{K}_P$ is diagonal, with identical components of 2000 N/m for both no-preload and preloaded cases. $\mathbf{K}_S$ is diagonal with identical components of 5 Nm/rad. The ratio between stiffness constants K_P/K_S is therefore equal to 400. The EE maintains its orientation while tracing the path. In Fig. 10, scaled-down translational stiffness ellipses are plotted at each point along the path to show the differences between parallel robots with and without flexures. The inner ellipses correspond to stiffness of the robot without preloads while the outer ones are for the flexure-based robot.

To quantitatively evaluate the stiffness improvement of the robot by adding preloaded flexures, the performance indices proposed in Sec. 5 are plotted (Fig. 11). The parallel robot with

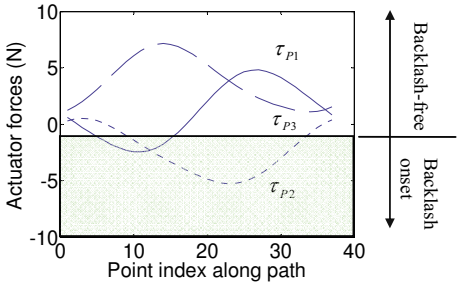

Fig. 9 Actuation force plots. The shaded region has the actuator backlash onset.

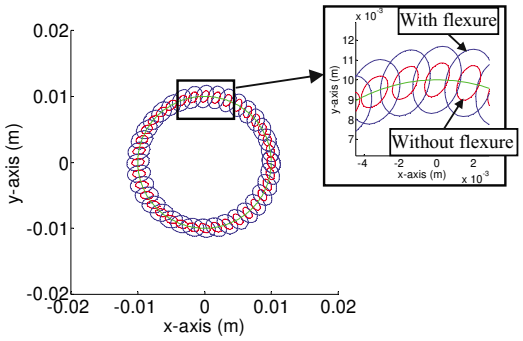

Fig. 10 Stiffness comparison between robots with and without flexures. The ratio of stiffness constants K_P/K_S is 400.

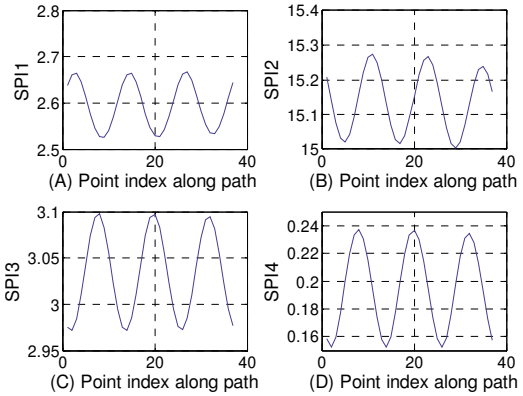

Fig. 11 Stiffness performance improvement plots of the robot while preloaded with flexures. Comparisons are along the circular path in Fig. 10.

flexures has better stiffness performances in all aspects, i.e., the Frobenius norm of the stiffness matrix (SPI1), the stiffness manipulability (SPI2), the overall stiffness measure (SPI3), and the stiffness isotropy (SPI4).

7 Experiments

The robot setup in Fig. 1 was constructed, as shown in Fig. 12(*a*). A multimedia extension describing this experimental setup and experiments of this section is available in [51]. Three Velmex linear slides were connected to Maxon servo motors, forming linear actuators. Torsional springs were assembled to the revolute joints between the moving platform and the legs, with their ends fixed to each side. The actual manufactured dimensions of the robot are as follows: the leg length is 100 mm, the moving platform has a side length 100 mm, and the travel of the actuators is 140 mm.

In order to illustrate the backlash prevention algorithm, an artificial backlash of 4 mm was created in the sliders, connecting the linear slides and the legs, as shown in Fig. 12(*b*). A pivot pin was press fit into the carriage of each linear actuator. The pin can rotate and translate in the slot of the corresponding slider. In operation, the torsional springs will load the legs against the advancing directions of the actuators and therefore close the backlash.

7.1 Calibration. The experimental setup is shown in Fig. 13(*a*). The robot was placed horizontally, with an optical tracker pointing vertically down at the robot. The tracker was from Claron Technology (H40), with the calibration accuracy of 0.20 mm root mean square (RMS) and the moving target accuracy of 0.14 mm RMS. An estimation of the actual tracking error was calculated as 0.25 mm RMS in Eq. (43). The tracker was connected to a laptop through FIREWIRE to read the positions of markers. As shown in Fig. 13(*b*), optical markers were classified into three categories. EE markers measured the position and orientation of the moving platform. Slide direction markers were used to calibrate the direction of each linear actuator. Slider markers provided the positions of the pivot pins. An external load was applied to the EE by using

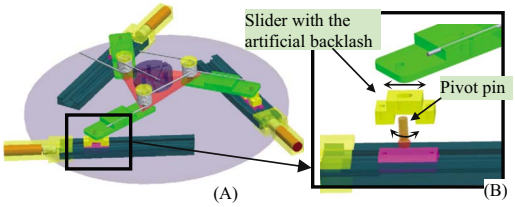

Fig. 12 Structure of the planar parallel robot: (*a*) CAD model; (*b*) exploded view of the robot's leg to show the artificial backlash

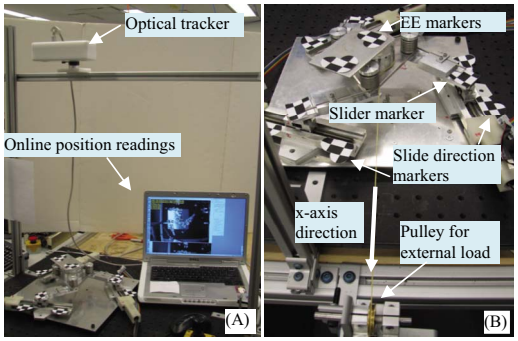

Fig. 13 Experimental setups: (*a*) position tracking system; (*b*) optical marker illustration and externally loaded robot setup

a calibration weight and a frictionless pulley. The direction of the load was defined as the positive x-axis (Fig. 13(*b*)).

$$\text{Error}_{\text{trac}} = \sqrt{0.20^2 + 0.14^2} = 0.25 \text{ mm} \tag{43}$$

7.2 Backlash Prevention. While without spring loads, the friction and assembly force ε within the slider was experimentally measured to be 1 N due to friction. The torsional springs were selected according to the simulation results and had a constant of 0.755 N m/rad.

Figure 14 shows the top views of the robot. In Fig. 14(*a*) the springs are free. In Fig. 14(*b*) the springs are preloaded and assembled to the robot legs. To determine the angle ψ_i corresponding to the free configuration of spring i, we digitized the spring ends in Fig. 14(*a*). Similarly, we digitized the spring ends in Fig. 14(*b*) when the springs were assembled. The results of our measurements are listed in Table 4. Using the spring constants, we found that the preload torsions were 0.94 N m, 0.97 N m, and 0.96 N m for springs 1, 2, and 3, respectively.

In the following experiments, we tested the robot's path tracing ability when assembled with or without preloaded springs.

7.2.1 Backlash Prevention Along a Specific Path. A circular path of 10 mm radius was specified for this experiment. The assembly position of the robot EE was taken as the starting point and the circular path centered at $[-10 \text{ mm}, 0, 0]^T$ away from the starting point. All points are defined in the tracker coordinate system. It was experimentally tested that the robot was more resistant to external loads in other directions than in the x-axis direction for its local 120 deg division. Therefore, an external force of 2 N along the x-axis was applied to the EE.

The robot traced the specified path while assembled with preloaded springs and without springs. For each case, five experi-

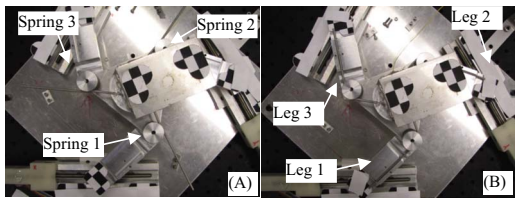

Fig. 14 Top view of spring angles: (*a*) no load; (*b*) preloaded

Table 4 Actual angles of springs

	γ (no load) (deg)	γ (with load) (deg)
Spring 1	−4.4	67
Spring 2	−4.5	69
Spring 3	−3.3	68.5

Spring angle definition

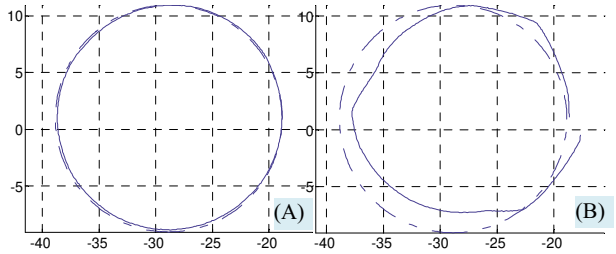

Fig. 15 Plots for tracing the 10 mm circle: (*a*) tracing plot with spring preloads; (*b*) tracing plot without spring preloads. In both plots, dashed curves represent the theoretical path and solid curves represent the actual tracing positions.

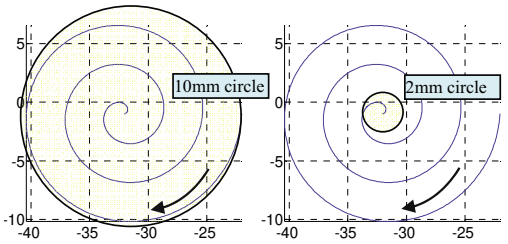

(A) Helical path tracing with external load of 2N along x-axis.

(B) Helical path tracing with external load of 2.5N along x-axis.

Fig. 18 Helical path plots. The shaded transparent regions show backlash-free target workspace for the corresponding external load.

ments were repeated. In Fig. 15, a comparison of tracing errors is shown, where the dashed curve represents the theoretical path and the solid curve represents the actual tracing positions. Figure 16 quantifies the tracing error by plotting the deviation from nominal values. The five curves close to the *x*-axis correspond to tracing errors with preloaded springs. The curves with large fluctuations depict the tracing errors without springs. The maximal position error of the EE was about 2 mm when the robot was not assembled with springs.

Using spring preload values of 0.94 N m, 0.97 N m, and 0.96 N m, we calculated the maximum allowable force to be 2 N, based on the algorithm in Sec. 4.1. Figure 17 shows the position tracing errors when the robot was subject to different loads. As shown in Fig. 17(*b*), the lower three curves correspond to 0 N, 1 N, and 2 N external loads. The upper curves, from bottom to top, correspond to 4 N, 10 N, and 14 N, respectively. When the external load was below 2 N, the three curves coincide with each other within the tracking error region. However, when the external force was equal to 4 N or above, backlash was noticeable in the robot and hence the path tracing error was increased. Note that as the load was always along *x*-axis, only backlash in slider 1 was triggered; therefore, the portion of curve with large tracing error corresponds to the backward motion of slider 1.

7.2.2 Backlash Prevention Within a Desired Workspace. In this experiment, the desired workspace was defined as the area circumvented by the circular path of 10 mm radius. As shown in Subsection 6.2.2, the path was scanned and the maximal force that can be applied to the robot was calculated to be 2 N (Fig. 18(*a*)). Likewise, a circular path of 2 mm radius around the circle center was scanned and the maximum allowable force without backlash onset was 2.5 N (Fig. 18(*b*)). A helical curve from the edge to the center was designed for the robot EE to trace, as shown in Fig. 18.

Figure 19(*a*) shows the position errors while the robot traced the helical path with different external loads. The plot can be divided into three regions as the designed helical curve was rotated three turns (1080 deg) about the center. As the radius of the tracing path was decreased, the position error also decreased. Figures 19(*b*) and 19(*c*) show that when the external loads were below 3 N, the tracing position error was always within the tracker error bound. When the load was 6 N, within the center circle of 2 mm radius, there was no backlash in the system (Fig. 19(*c*)). However, in the workspace outside of the 2 mm circle, the backlash was noticeable (Fig. 19(*b*)). It means that the load of 6 N represents a critical value which allows no backlash only in the

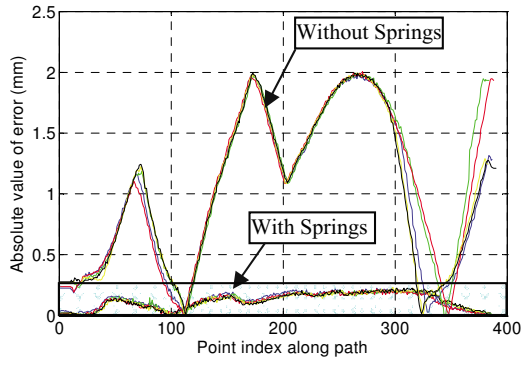

Fig. 16 Tracing error plots. The shaded transparent region represents the upper bound of the tracker errors.

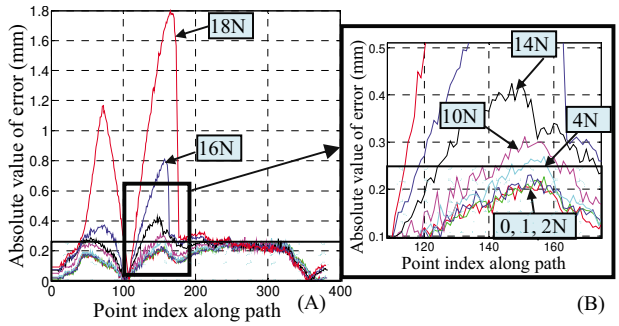

Fig. 17 Tracing error plots for different external loads. The transparent regions represent the upper bound of the tracker errors.

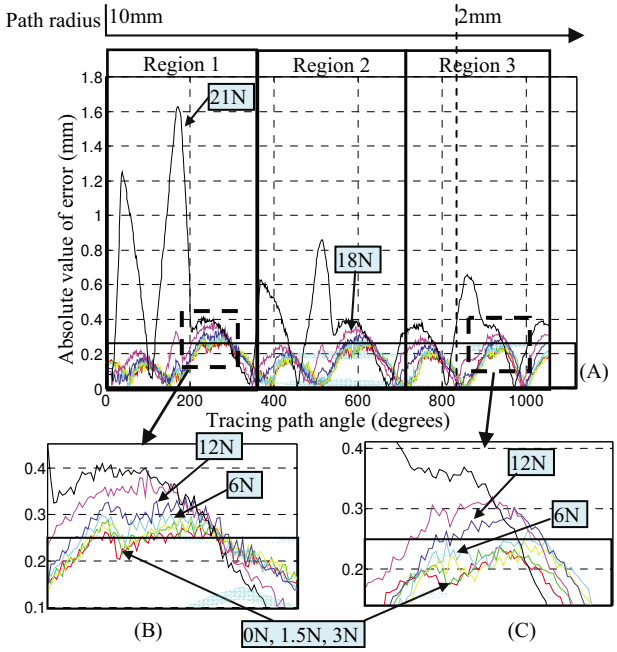

Fig. 19 Position errors when the robot traced the helical path with different loads. The transparent regions represent the upper bound of the tracker errors.

inner portion of the workspace. When the external load was 12 N or above, it is clear that throughout the three regions, backlash is observable. Note that the critical load of 6 N is greater than the theoretical value calculated earlier based on the algorithm, which was 2.5 N. This is because the proposed algorithm has some margin while determining the preload requirements, as was verified in the simulation in Sec. 6.2.

8 Conclusion

This paper presented the design of planar parallel robots preloaded with torsional springs (flexure joints). For a proposed case-study robot, statics, singularity, backlash prevention, and stiffness modeling were investigated. An algorithm was put forward to determine the preload conditions while the robot traced a specific path and moved within a desired workspace subject to a norm-bounded wrench, and this algorithm was experimentally validated. For the stiffness analysis, an explicit expression of the robot's stiffness matrix was derived. Moreover, stiffness performance indices were proposed by using the vertex linear velocities to replace the general EE twist, in order to generate more homogeneous stiffness matrix in terms of physical units. The robot's stiffness features were examined in simulation. The results presented in this paper can be used for robot design in order to determine the connection geometry of the flexure joints to the moving platform. Also, using this method, it is possible to construct inexpensive backlash-free parallel robots using regular joints preloaded with springs.

References

[1] Pollard, W., 1942, "Position Controlling Apparatus," U.S. Patent No. 2,236,571.

[2] Stewart, D., 1965, "A Platform With 6 Degrees of Freedom," Proc. Inst. Mech. Eng., **180**, pp. 371–386.

[3] Bamberger, H., Wolf, A., and Shoham, M., 2008, "Assembly Mode Changing in Parallel Mechanisms," IEEE Trans. Rob., **24**(4), pp. 765–772.

[4] Alici, G., and Shirinzadeh, B., 2005, "Vibration Analysis of Piezo-Actuated Flexure-Jointed Mechanisms," Proc. SPIE, **5649**(2), pp. 445–453.

[5] Ohya, Y., Arai, T., Mae, Y., Inoue, K., and Tanikawa, T., 1999, "Development of 3-DOF Finger Module for Micro Manipulation," *Proceedings of the IEEE International Conference on Intelligent Robots and Systems*, pp. 894–899.

[6] Yan, S., Zhang, F., Qin, Z., and Wen, S., 2006, "A 3-DOFs Mobile Robot Driven by a Piezoelectric Actuator," Smart Mater. Struct., **15**(1), pp. N7–N13.

[7] Howell, L. L., 2001, *Compliant Mechanisms*, Wiley, New York.

[8] Lobontiu, N., 2003, *Compliant Mechanisms Design of Flexure Hinges*, CRC, Boca Raton, FL.

[9] Pham, H.-H., and Chen, I.-M., 2005, "Micro-Motion Selective-Actuation X Y Z Flexure Parallel Mechanism: Design and Modeling," Journal of Micromechatronics, **3**(1), pp. 51–73.

[10] Trease, B. P., Moon, Y.-M., and Kota, S., 2005, "Design of Large-Displacement Compliant Joints," ASME J. Mech. Des., **127**(4), pp. 788–798.

[11] Chen, I.-M., 2002, "Kinematics, Workspace and Static Analyses of Two DOF Flexure Parallel Mechanism," *Proceedings of the Seventh Intertional Conference on Control, Automation, Robotics and Vision*, Singapore, pp. 968–973.

[12] Oetomo, D., Daney, D., Shirinzadeh, B., and Merlet, J.-P., 2008, "Certified Workspace Analysis of 3RRR Planar Parallel Flexure Mechanism," *Proceedings of the IEEE International Conference on Robotics and Automation*, Pasadena, CA, pp. 3838–3843.

[13] Xu, Q., and Li, Y., 2006, "A Novel Design of a 3-PRC Translational Compliant Parallel Micromanipulator for Nanomanipulation," Robotica, **24**(4), pp. 527–528.

[14] Kang, B. H., Wen, J. T.-Y., Dagalakis, N. G., and Gorman, J. J., 2005, "Analysis and Design of Parallel Mechanisms With Flexure Joints," IEEE Trans. Rob., **21**(6), pp. 1179–1184.

[15] Yi, B.-J., Chung, G. B., Na, H. Y., Kim, W. K., and Suh, I. H., 2003, "Design and Experiment of a 3-DOF Parallel Micromechanism Utilizing Flexure Hinges," IEEE Trans. Rob. Autom., **19**(4), pp. 604–612.

[16] Awtar, S., and Slocum, A. H., 2007, "Constraint-Based Design of Parallel Kinematic XY Flexure Mechanisms," ASME J. Mech. Des., **129**(8), pp. 816–830.

[17] Bacher, J. P., Bottinelli, S., Breguet, J. M., and Clavel, R., 2001, "Delta3: Design and Control of a Flexure Hinges Mechanism," Proc. SPIE, **4568**, pp. 135–142.

[18] Cash, M., Bruch, D., Jahn, B., and Keas, P., 2008, "Practical Considerations of Joint Friction and Backlash in Large Ground-Based Telescope Secondary Optic Positioning Systems," Proc. SPIE, **7018**, pp. 1–12.

[19] Zubir, M. N. M., and Shirinzadeh, B., 2008, "Development of a Compliant-Based Microgripper for Microassembly," *Proceedings of the 2008 IEEE/ASME International Conference on Mechtronic and Embedded Systems and Applications (MESA)*, Piscataway, NJ, pp. 522–527.

[20] Hesselbach, J., and Raatz, A., 2000, "Pseudo-Elastic Flexure-Hinges in Robots for Micro Assembly," Proc. SPIE, **4194**, pp. 157–167.

[21] Dong, W., Sun, L., and Du, Z., 2008, "Stiffness Research on a High-Precision, Large-Workspace Parallel Mechanism With Compliant Joints," Precis. Eng., **32**(3), pp. 222–231.

[22] Awtar, S., Slocum, A. H., and Sevincer, E., 2007, "Characteristics of Beam-Based Flexure Modules," ASME J. Mech. Des., **129**(6), pp. 625–639.

[23] Lan, C.-C., and Cheng, Y.-J., 2008, "Distributed Shape Optimization of Compliant Mechanisms Using Intrinsic Functions,"ASME J. Mech. Des., **130**(7), p. 072304.

[24] Kock, S., and Schumacher, W., 1998, "A Parallel X-Y Manipulator With Actuation Redundancy for High-Speed and Active-Stiffness Applications," *Proceedings of the IEEE International Conference on Robotics and Automation*, pp. 2295–2300.

[25] Yi, B.-J., and Freeman, R. A., 1992, "Synthesis of Actively Adjustable Springs by Antagonistic Redundant Actuation," ASME J. Dyn. Syst., Meas., Control, **114**(3), pp. 454–461.

[26] Muller, A., 2005, "Internal Preload Control of Redundantly Actuated Parallel Manipulators—Its Application to Backlash Avoiding Control," IEEE Trans. Rob., **21**(4), pp. 668–677.

[27] Pashkevich, A., Chablat, D., and Wenger, P., 2008, "Stiffness Analysis of 3-D.O.F. Overconstrained Translational Parallel Manipulators," *Proceedings of the IEEE International Conference on Robotics and Automation*, pp. 1562–1567.

[28] Pham, H.-H., and Chen, I.-M., 2005, "Stiffness Modeling of Flexure Parallel Mechanism," Precis. Eng., **29**(4), pp. 467–478.

[29] Simaan, N., and Shoham, M., 2003, "Stiffness Synthesis of a Variable Geometry Six-Degree-of-Freedom Double Planar Parallel Robot," Int. J. Robot. Res., **22**(9), pp. 757–775.

[30] Zhang, D., and Gosselin, C. M., 2001, "Kinetostatic Modeling of N-DOF Parallel Mechanisms With a Passive Constraining Leg and Prismatic Actuators," ASME J. Mech. Des., **123**(3), pp. 375–381.

[31] Chen, S.-F., and Cao, I., 2000, "Conservative Congruence Transformation for Joint and Cartesian Stiffness Matrices of Robotic Hands and Fingers," Int. J. Robot. Res., **19**(9), pp. 835–847.

[32] Kövecses, J., and Angeles, J., 2007, "The Stiffness Matrix in Elastically Articulated Rigid-Body Systems," Multibody Syst. Dyn., **18**(2), pp. 169–184.

[33] Quennouelle, C., and Gosselin, C. M., 2008, "Stiffness Matrix of Compliant Parallel Mechanisms," *Advances in Robot Kinematics: Analysis and Design*, Springer, New York, pp. 331–341.

[34] Angeles, J., 2002, *Fundamentals of Robotic Mechanical Systems, Mechanical Engineering Series*, Springer, New York.

[35] Angeles, J., and Lopez-Cajun, C. S., 1992, "Kinematic Isotropy and the Conditioning Index of Serial Robotic Manipulators," Int. J. Robot. Res., **11**(6), pp. 560–571.

[36] Lee, J., 1997, "A Study on the Manipulability Measures for Robot Manipulators," *Proceedings of the IEEE/RSJ International Conference on Intelligent Robots and Systems*, Grenoble, France, pp. 1458–1465.

[37] Yoshikawa, T., 1985, "Manipulability of Robotic Mechanisms," Int. J. Robot. Res., **4**(2), pp. 3–9.

[38] Valasek, M., Belda, K., and Florian, M., 2002, "Control and Calibration of Redundantly Actuated Parallel Robots," *Proceedings of the Third Parallel Kinematics Seminar*, Chemnitz, pp. 411–427.

[39] Merlet, J.-P., 2006, *Parallel Robots*, Springer, Dordrecht, The Netherlands.

[40] Cleary, K., and Uebel, M., 1994, "Jacobian Formulation for a Novel 6-DOF Parallel Manipulator," *Proceedings of the IEEE International Conference on Robotics and Automation*, pp. 2377–2382.

[41] Simaan, N., Glozman, D., and Shoham, M., 1998, "Design Considerations of New Six Degrees-of-Freedom Parallel Robots," *Proceedings of the IEEE International Conference on Robotics and Automation*, pp. 1327–1333.

[42] Arora, J. S., 2004, *Introduction to Optimum Design*, Academic, CA.

[43] Simaan, N., 2002, "Task-Based Design and Synthesis of Variable Geometry Parallel Robots," Ph.D. thesis, Technion, Haifa, Isarel.

[44] Bicchi, A., and Prattichizzo, D., 2000, "Manipulability of Cooperating Robots With Unactuated and Closed-Chain Mechanisms," IEEE Trans. Robot. Autom., **16**(4), pp. 336–345.

[45] Chiacchio, P., Chiaverini, S., Sciavicco, L., and Siciliano, B., 1991, "Global Task Space Manipulability Ellipsoids for Multiple-Arm Systems," IEEE Trans. Robot. Autom., **7**(5), pp. 678–685.

[46] Fattah, A., and Hasan Ghasemi, A. M., 2002, "Isotropic Design of Spatial Parallel Manipulators," Int. J. Robot. Res., **21**(9), pp. 811–824.

[47] Gosselin, C., 1992, "The Optimum Design of Robotic Manipulators Using Dexterity Indices," Rob. Auton. Syst., **9**(4), pp. 213–226.

[48] Gosselin, C. M., and Angeles, J., 1991, "A Global Performance Index for the Kinematic Optimization of Robotic Manipulators," ASME J. Mech. Des., **113**(3), pp. 220–226.

[49] Merlet, J.-P., 2006, "Jacobian, Manipulability, Condition Number, and Accuracy of Parallel Robots," ASME J. Mech. Des., **128**(1), pp. 199–206.

[50] Park, F., and Brockett, R., 1994, "Kinematic Dexterity of Robotic Mechanisms," Int. J. Robot. Res., **13**(1), pp. 1–15.

[51] Wei, W., and Simaan, N., "Multimedia Extension: Design of Planar Parallel Robots With Preloaded Flexures for Guaranteed Backlash Prevention," http://www.columbia.edu/cu/mece/arma/projects/BP/BP.shtml